Journal of Materials Science: Materials in Electronics (2019) 30:10923–10933
https://doi.org/10.1007/s10854-019-01436-4

Enhanced visible-light responsive photocatalytic activity of $Bi_{25}FeO_{40}$/$Bi_2Fe_4O_9$ composites and mechanism investigation

Geming Wang[1] · Da Cheng[1] · Tiancheng He[1] · Yiyu Hu[1] · Quanrong Deng[1] · Yangwu Mao[1] · Shenggao Wang[1]

Received: 23 January 2019 / Accepted: 29 April 2019 / Published online: 3 May 2019
© Springer Science+Business Media, LLC, part of Springer Nature 2019

Abstract
Pure $Bi_{25}FeO_{40}$, $Bi_2Fe_4O_9$, and different weight ratios of $Bi_{25}FeO_{40}$/$Bi_2Fe_4O_9$ composite photocatalysts have been synthesized via a hydrothermal process combined with a mixing-calcination method and evaluated as visible-light responsive catalyst for the degradation of Rhodamine B (RhB). All the as-prepared samples have been characterized by a range of techniques including X-ray diffraction (XRD), Fourier transform infrared spectra (FT-IR), UV–vis absorption spectra (DSR), Field Emission Scanning Electron Microscope (FE-SEM), Transmission electron microscope (TEM) and High-resolution TEM (HRTEM). The XRD, FT-IR, TEM and HRTEM results confirm that the composite only consists of $Bi_{25}FeO_{40}$ and $Bi_2Fe_4O_9$. In the $Bi_{25}FeO_{40}$/$Bi_2Fe_4O_9$ composites, closely contacted interfaces have been observed. Compared with the single-phase $Bi_{25}FeO_{40}$ and $Bi_2Fe_4O_9$, $Bi_{25}FeO_{40}$/$Bi_2Fe_4O_9$ composites exhibit enhanced visible-light responsive photocatalytic activities. The photocatalytic efficiency of optimized $Bi_{25}FeO_{40}$/$Bi_2Fe_4O_9$ composite with $Bi_2Fe_4O_9$ weight ratio of 30% is about 8.8 and 6.2 times higher than that of pure $Bi_{25}FeO_{40}$ and $Bi_2Fe_4O_9$, respectively. On the basis of electronic energy-band structure analysis, the active species trapping experiments and the electrochemical impedance spectrum (EIS) performance, a heterojunction-type charge transfer mechanism interpreting the enhanced photocatalytic activities of the composite are proposed and discussed. In addition, the effects of different $Bi_{25}FeO_{40}$/$Bi_2Fe_4O_9$ weight ratios and their geometry architecture on photocatalytic activities are also thoroughly discussed.

1 Introduction

As a family of environment-friendly metal oxide, Bismuth ferrite (BFO) displays outstanding characteristics including multiferroic [1, 2], electronic [3], optical [4], and gas-sensoring properties [5] in the past decades. Recently, BFO has also obtained wide attentions as a visible-light-driven semiconductor photocatalysis candidate because they have owned fascinating abilities in terms of photodegradation of organic pollutants, photocatalytic water splitting, photovoltaic and photoelectrochemical conversion [6–9]. They have three types of crystalline phases: perovskite-type $BiFeO_3$, mullite-type $Bi_2Fe_4O_9$ and selenite-type $Bi_{25}FeO_{40}$. By virtue of narrowing band gaps of about 2.2 eV and 1.7-2.2 eV respectively, both perovskite-type $BiFeO_3$ and mullite-type $Bi_2Fe_4O_9$ are found to be sensitive to visible light and exhibit visible-light responsive photocatalytic capacity for the decomposition of Rhodamine B, Congo red, Bisphenol A and other organic pollutions [10–13]. Meanwhile, selenite-type $Bi_{25}FeO_{40}$ with a suitable bandgap (< 2.8 eV) features in a body-centered cubic structure (the cubic space group I23), which favors an eminent mobility of photo-generated charges, good nonlinear optical effect and great optical response, making it also an ideal visible-light-driven photocatalysis [14–16]. However, the visible-light responsive photocatalytic efficiency of single-component BFO are not very impressive due to the low quantum efficiency, the fast recombination of photogenerated electron–hole pairs and the inefficient light absorption, all of which restrict its practical application [6].

In general, it is still a great challenge to prepare phase-purity BFO structure owing to the kinetics of phase formation of Bi_2O_3/Fe_2O_3 and the high volatility of bismuth [17]. Thermodynamic studies demonstrate that the appearance of $Bi_2Fe_4O_9$, $Bi_{25}FeO_{40}$, Bi_2O_3 or Fe_2O_3 as by-products is difficult to be completely eliminated during the preparation of $BiFeO_3$ [18]. On the contrary, the phase evolution from

✉ Geming Wang
wanggemingwit@163.com

[1] Hubei Key Laboratory of Plasma Chemistry and Advanced Materials, School of Materials Science and Engineering, Wuhan Institute of Technology, Wuhan, People's Republic of China

$Bi_2Fe_4O_9$ to $BiFeO_3$ and then to $Bi_{25}FeO_{40}$ in a wide temperature range between 720 K and 1040 K is experimentally observed during the hydrothermal synthesis of BFO as long as the process parameters are changed [19–21]. It is notable that the presence of BFO impurities in Bi_2O_3/Fe_2O_3 system will bring charge unbalance and structure defects, resulting in the deterioration of its functional properties [22–24]. In terms of promoting photocatalytic activity of pure BFO, copious efforts have been exploited mainly including tailoring morphology [14, 25–27], controlling exposed facets [12, 13], reducing dimension [8, 28, 29] and doping with metal or nonmetal ions [30–32]. For example, Ji et al. also synthesize $Bi_{25}FeO_{40}$ microtetrahedra, microcubes and microsphere respectively, and the microcubes exhibit 88% photo-Fenton photocatalytic degradation of RhB within 120 min due to its exposed (001) facets with the active O atoms [14]. Hao et al. and Gao et al. demonstrate that reducing the particle size of $BiFeO_3$ can obviously improve its photocatalytic activity, which is mainly ascribed to the increased surface active catalytic-sites and the shortened migrate distances of photogenerated carriers [28, 29]. More importantly, the mixed-phase structure, that is, the coexistence of BFO main phase and BFO impurities, is found to be beneficial to favor the visible light harvesting and boost photocatalytic activity compared to that of pure phases [13, 24, 33–37]. Yang et al. observe that mixed-phase $BiFeO_3/Bi_2Fe_4O_9$ nanoflakes show much better photocatalytic activities than that of pure BFO, which could completely degrade RhB within 240 min under UV irradiation [33]. Similar results have also been found in the $BiFeO_3/Bi_2Fe_4O_9$ composites with 71.45% degradation rate of Congo red in 90 min owing to the formation of hybrid structure and large specific surface area [13]. Since impurities seem to be unavoidable, a novel and feasible strategy in further improving photocatalytic property of BFO is to utilize impurities to construct heterojunction comprising BFO main phase and BFO impurities via a semiconductor coupling technology. Coupling of two semiconductor photocatalysis with staggered alignment of band structures can not only dominate the transport direction, but also effectively facilitate the separation of photogenerated electrons/holes, leading to the enhancement of photocatalytic and electrochemical property [37–41]. For instance, Wang's group discovers that PtO coupled g-C_3N_4 exhibit excellent hydrogen production performance, which is mainly due to the strong interaction between the co-catalyst and the host g-C_3N_4 [38]. Zhao and coworkers design novel $Bi_4Ti_3O_{12}/Bi_2Ti_2O_7$ heterostructure nanofibers and observe a dramatic enhancement in the photocatalytic hydrogen evolution activity, which can be ascribed to the internal electric field formed in this composite [41]. Moreover, Zhang et al. synthesize 3D hierarchical $CoWO_4/Co_3O_4$ structure with the synergetic effect of diverse materials and fast transmission of electrons and ions, demonstrating a high superior rate capability [39]. Following this strategy, Kong et al. find that $BiFeO_3/(Bi/Fe)_2O_3$ heterojunction displays 2.5 times higher photocatalytic destruction of gaseous toluene than bare $BiFeO_3$, which can be ascribed to carrier transfer between $BiFeO_3$ and $(Bi/Fe)_2O_3$ interfaces over nano junctions [35]. Recently, $BiFeO_3/Bi_2Fe_4O_9$ heterojunction nanofibers have also commendable photocatalytic capacity due to a Z-Scheme mechanism based on the results of electronic energy-band structure analysis [7]. Similar phenomena have also been reported in other Bi-based semiconductor photocatalysis [42, 43]. Very recently, Xia's group prepares an n-$SrTiO_3$/p-BiOI heterojunction by loading $SrTiO_3$ particles onto the surface of BiOI nanoflakes via a two-step method. The obtained n-$SrTiO_3$/p-BiOI composite exhibits excellence photocatalytic performance for the degradation of crystal violet solution [42].

Up till now, there have been seldom reports on $Bi_{25}FeO_{40}/Bi_2Fe_4O_9$ composites. Herein, a novel $Bi_{25}FeO_{40}/Bi_2Fe_4O_9$ composite will be necessary to be systematically investigated for offering new insight into the design and application of BFO based high-efficiency photocatalyst. Inspired by the above facts, a series of $Bi_{25}FeO_{40}/Bi_2Fe_4O_9$ composites were synthesized via the method of facile hydrothermal route and mixing-calcination in this paper. Various techniques including XRD, FI-TR, SEM, TEM (HRTEM) and UV–vis DSR are employed to characterize phase structure, microstructure and optical properties of as-prepared samples. The visible-light responsive photocatalytic activities of Rhodamine B (RhB) over $Bi_{25}FeO_{40}/Bi_2Fe_4O_9$ composites are evaluated, and the optimal weight ratio of $Bi_2Fe_4O_9$ to $Bi_{25}FeO_{40}$ is determined. The $Bi_{25}FeO_{40}/Bi_2Fe_4O_9$ composites exhibit much higher visible-light responsive photodegradation efficiency of RhB than that of pure $Bi_{25}FeO_{40}$ and $Bi_2Fe_4O_9$ respectively. The heterojunction-type photocatalytic mechanism is proposed to interpret charge transfer across $Bi_{25}FeO_{40}/Bi_2Fe_4O_9$ interfaces, as evidenced by the energy band gap structure analysis, the reactive species trapping experiments and the electrochemical impedance spectra (EIS) measurements. The effects of $Bi_{25}FeO_{40}/Bi_2Fe_4O_9$ weight ratios on photocatalytic activities of composites are thoroughly investigated.

2 Experimental

2.1 Synthesis

The chemical reagents, that is, $Bi(NO_3)_3{\cdot}5H_2O$, $Fe(NO_3)_3{\cdot}9H_2O$, HNO_3 solution, NaOH mineralizer and KNO_3 additive, were used to synthesize pure-phase $Bi_{25}FeO_{40}$ and $Bi_2Fe_4O_9$ powders via a simple hydrothermal process. All the chemicals were of analytical grade and used without further purifications. For preparing $Bi_{25}FeO_{40}$, 12 mmol $Bi(NO_3)_3{\cdot}5H_2O$ and 1 mmol $Fe(NO_3)_3{\cdot}9H_2O$ were

dissolved and stirred in 20 ml HNO_3 solution. Subsequently, the NaOH solution with the concentration of 4 M was slowly added in the solution until the Fe^{3+} and Bi^{3+} ions were deposited completely under continuous stirring. The precipitates were withdrawn and washed repeatedly by distilled water before being dissolved in 4 M NaOH solution again. Next, 0.05 mol KNO_3 was added into the above solution to control morphology of products. After 1 h of stirring, the mixtures were poured into a stainless-steel Teflonlined reactor, and then heated at 180 °C for 12 h. The powders were finally obtained by centrifugation, being washed several times with water and alcohol, and being dried at 80 °C for 6 h. The $Bi_2Fe_4O_9$ samples were synthesized using the same hydrothermal procedure except for an initial Bi/Fe ratio of 1:2 (1 mmol $Bi(NO_3)_3{\cdot}5H_2O$ and 2 mmol $Fe(NO_3)_3{\cdot}9H_2O$) [34]. The $Bi_{25}FeO_{40}/Bi_2Fe_4O_9$ composites were fabricated by a facile mixing-calcination method: a certain amount of $Bi_2Fe_4O_9$ and $Bi_{25}FeO_{40}$ powders were mixed, thoroughly grounded in an agate mortar and heated at 300 °C for 1 h. In this manner, the obtained products with different weight ratios of $Bi_2Fe_4O_9$ to $Bi_{25}FeO_{40}/Bi_2Fe_4O_9$ composite at 0% (pure $Bi_{25}FeO_{40}$), 10, 30, 50 and 100% (pure $Bi_2Fe_4O_9$) were defined as S1, S2, S3, S4 and S5 respectively.

2.2 Characterization

X-ray powder diffraction (XRD) measurements of samples were identified on Philips X'pert PW3373/10 diffractometer by employing Cu *K*αradiation (λ = 1.5406 Å) in the 2θ range of 10–80° to identify crystal structures. Fourier transform infrared spectra (FT-IR) of powders were recorded in a Nicolet 6700 spectrophotometer with the wavelength ranging from 400 to 4000 cm^{-1} at room temperature. The morphology and microcrystalline structure characteristics of samples were performed by a Field Emission Scanning Electron Microscope (FE-SEM, HITACHI UHR FE-SEM SU8000), High-resolution TEM (HRTEM, JEM-2100, JEOL). UV–vis absorption spectra (DSR) of as-prepared powders were measured on a UV–vis spectrophotometer (UV2550, Shimadzu). The photoelectrochemical test was carried out using a typical three-electrode cell on CHI760 electrochemical workstation (Shanghai Chenhua Instrument Co. Ltd). The obtained photocatalysts thin films covered on fluorine-doped tin oxide (FTO) glass by using drop-casting method were used as working electrode. A platinum wire was used as counter electrode, and a saturation calomel electrode (SCE) served as the reference electrode respectively. The 0.5 M Na_2SO_4 solution was used as electrolyte.

2.3 Photocatalytic activity

The visible-light-driven photocatalytic activities of pure $Bi_{25}FeO_{40}$, $Bi_2Fe_4O_9$ and a series of $Bi_{25}FeO_{40}/Bi_2Fe_4O_9$ composites were evaluated by degradation of RhB aqueous solution. A 500 W Xe lamp equipped with a cutoff filter (λ > 420 nm) was employed as the visible light source. 100 mg photocatalysis was dispersed in 100 mL of 10 mg/L RhB aqueous solution. Before irradiation, the suspension was continuously stirred in dark for 1 h to get absorption–desorption equilibrium between the photocatalysis and RhB. At every 1 h time interval, 3 ml of the suspension was taken from the reactor and centrifuged at 12,000 rpm for 30 min, then analyzed on UV–vis spectrophotometer at a wavelength of 533 nm to determine the RhB concentration. Active species capturing experiments over $Bi_{25}FeO_{40}/Bi_2Fe_4O_9$ composite were also carried out during the identical photocatalytic procedure by adding 1 mmol scavengers, namely, 2-propanol (IPA), pbenzoquinone (BQ) and disodium ethylenediamine tetraacetic acid (EDTA-2Na), into the RhB solution to trap hydroxyl radicals (·OH), superoxide radicals ($\cdot O_2^-$) and holes (h^+) respectively [44].

3 Results and discussion

3.1 XRD and FT-IR analysis

Figure 1 shows X-ray diffraction patterns of $Bi_{25}FeO_{40}$, $Bi_2Fe_4O_9$ and $Bi_{25}FeO_{40}/Bi_2Fe_4O_9$ composites. For pure $Bi_{25}FeO_{40}$ and $Bi_2Fe_4O_9$, all characteristic diffraction peaks can be perfectly indexed to the single-phase orthorhombic structure $Bi_2Fe_4O_9$ (JCPDS card No. 74-1098) and body-centered cubic structure $Bi_{25}FeO_{40}$ (JCPDS card No. 46-0416) respectively, which retains consistency with previous literatures [9, 12]. The sharp diffraction peaks in their spectra indicate that they are highly-crystallized. The characteristic diffraction peaks of $Bi_{25}FeO_{40}/Bi_2Fe_4O_9$ composites

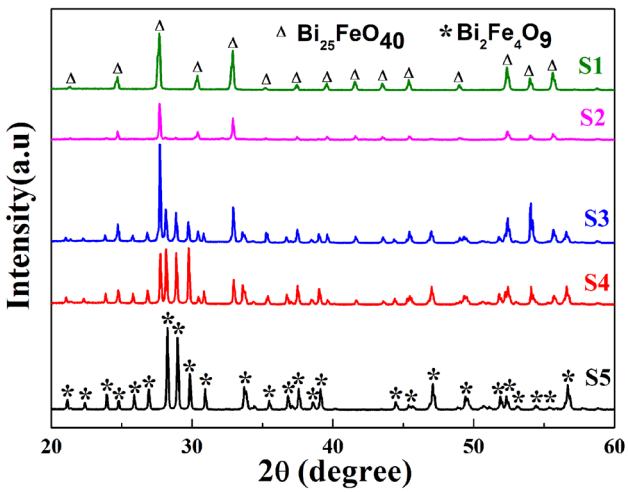

Fig. 1 The XRD patterns of pure $Bi_{25}FeO_{40}$, $Bi_2Fe_4O_9$, and $Bi_{25}FeO_{40}/Bi_2Fe_4O_9$ composites

does not change greatly and can be also in good agreement with either cubic $Bi_{25}FeO_{40}$ or orthorhombic $Bi_2Fe_4O_9$, displaying the coexistence of $Bi_{25}FeO_{40}$ and $Bi_2Fe_4O_9$ in the composites. No other impurity peaks are found, further confirming that the composites are two phases system [45]. However, although the XRD pattern of the sample S2 is quite similar to that of pure $Bi_{25}FeO_{40}$, it possess some weak diffraction peaks of $Bi_2Fe_4O_9$ (28.2° and 28.9°), which is probably due to the low content of $Bi_2Fe_4O_9$ and the overlapped peaks between $Bi_{25}FeO_{40}$ and $Bi_2Fe_4O_9$ in the composite [46]. As predicted, the intensity of the three most intense $Bi_2Fe_4O_9$ peaks at about 28.2°, 28.9° and 29.8°, which correspond to (121), (211) and (002) crystalline orientations, increases obviously with increasing $Bi_2Fe_4O_9$ content in the composites. As a consequence, the XRD results suggest that $Bi_{25}FeO_{40}/Bi_2Fe_4O_9$ composites are successfully fabricated.

The FT-IR spectra of $Bi_{25}FeO_{40}$, $Bi_2Fe_4O_9$ and $Bi_{25}FeO_{40}/Bi_2Fe_4O_9$ composites are presented in Fig. 2. In the spectra of $Bi_{25}FeO_{40}$, three main absorption bands in the region 400–700 cm^{-1} are attributed to the typical absorption bands for the Bi–O and Fe–O [15]. The strong absorptive peaks located at 461 and 522 cm^{-1} are assigned to Bi–O vibration modes and the remaining peak at 578 cm^{-1} is associated with the stretching vibration of Fe–O bond, demonstrating the cubic characteristic of sillenite-type $Bi_{25}FeO_{40}$ [47]. The peak around 1322 cm^{-1} is due to the stretching vibration of C–OH [48]. With respect to $Bi_2Fe_4O_9$, the peaks in the range from 444 to 473 cm^{-1} being assigned to Fe–O stretching vibrations in the FeO_6 octahedral, the peaks at 640 and 810 cm^{-1} corresponding to Fe–O stretching vibrations in the FeO_6 tetrahedral, and the appearance of absorption peaks around 523 and 609 cm^{-1} being attributed to O–Fe–O and Fe–O–Fe bending vibration in the FeO_4 tetrahedral, all of these reflect the orthorhombic characteristic of mullite-type $Bi_2Fe_4O_9$ [49]. Furthermore, these observed peaks of pure $Bi_{25}FeO_{40}$ and $Bi_2Fe_4O_9$ are detected and overlapped in the $Bi_{25}FeO_{40}/Bi_2Fe_4O_9$ composites, confirming that $Bi_2Fe_4O_9$ is composited well with $Bi_{25}FeO_{40}$ in our final samples. With the increase of $Bi_2Fe_4O_9$ content from the sample S2 to S4, the FT-IR peaks of $Bi_2Fe_4O_9$ (e.g. 640 and 810 cm^{-1}) increase and $Bi_{25}FeO_{40}$ (e.g. 522 and 578 cm^{-1}) decrease and even disappear, which is similar to those of g-C_3N_4/Bi_2MoO_6, g-C_3N_4/$SmVO_4$ and g-C_3N_4/$BiFeO_3$ composites [50–52]. Those results are in accordance with our XRD results.

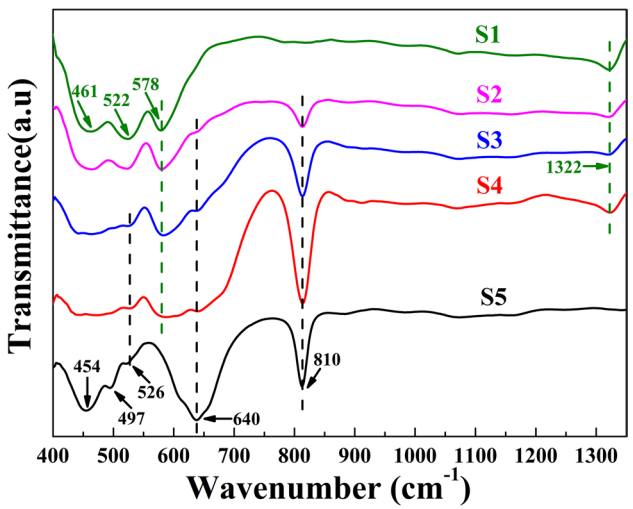

Fig. 2 The FT-IR spectra of pure $Bi_{25}FeO_{40}$, $Bi_2Fe_4O_9$, and $Bi_{25}FeO_{40}/Bi_2Fe_4O_9$ composites

3.2 SEM and TEM observations

Figure 3 demonstrates FE-SEM images of $Bi_{25}FeO_{40}$, $Bi_2Fe_4O_9$ and $Bi_{25}FeO_{40}/Bi_2Fe_4O_9$ composites, which reflect different morphology and surface textural. Apparently, pure $Bi_{25}FeO_{40}$ particles present cubic morphology with an average size of about 10 μm and its surfaces are smooth (Fig. 3a). In Fig. 3e, pure $Bi_2Fe_4O_9$ particles have a sheet-like appearance with ca. 2 μm in length and width [34]. After surface decorating with $Bi_2Fe_4O_9$ in the samples, as shown in Fig. 3c, the FE-SEM image clearly shows that smaller $Bi_2Fe_4O_9$ microsheets homogeneously anchor on and tightly attached to the whole surface of bigger $Bi_{25}FeO_{40}$ microcubes, which leads to the successful formation $Bi_{25}FeO_{40}/Bi_2Fe_4O_9$ heterojunctions. However, when the content of $Bi_2Fe_4O_9$ decreases, $Bi_2Fe_4O_9$ microsheets randomly disperse on the surface of $Bi_{25}FeO_{40}$ microcubes and some of cubes are barren (Fig. 3b), implying the limited formation of $Bi_{25}FeO_{40}/Bi_2Fe_4O_9$ hybrid. Conversely, the excessive amount of $Bi_2Fe_4O_9$ in the composite leads to thick $Bi_2Fe_4O_9$ layer growing on the $Bi_{25}FeO_{40}$ microcubes (Fig. 3d), which has been proven to be harmful for photodegradation process [48, 53, 54]. The different $Bi_{25}FeO_{40}/Bi_2Fe_4O_9$ weight ratios in the composites have a major influence on photocatalytic behavior optimizing, which will be thoroughly discussed below. The detailed microstructural features of $Bi_{25}FeO_{40}/Bi_2Fe_4O_9$ composite are further characterized by and TEM and HRTEM analysis, and the sample S3 is taken as an example. As shown in Fig. 4a, the sample S3 consists of cubic texture of micro-sized $Bi_{25}FeO_{40}$ tightly surrounded by small $Bi_2Fe_4O_9$ microsheets, which is consistent with our SEM results. Meanwhile, the HRTEM image is also displayed in Fig. 4b. The two types of clear lattice fringes demonstrate the coexisting of $Bi_{25}FeO_{40}$ and $Bi_2Fe_4O_9$, in which the 0.273 nm and 0.220 nm of interplanar spacing are in good agreement with the (321) plane of selenite-type $Bi_{25}FeO_{40}$ and (212) plane of mullite-type $Bi_2Fe_4O_9$, respectively [44, 54]. Considering the ultrasonication treatment of TEM sample preparation, it is inferred that there are intimate interfaces and strong interaction between

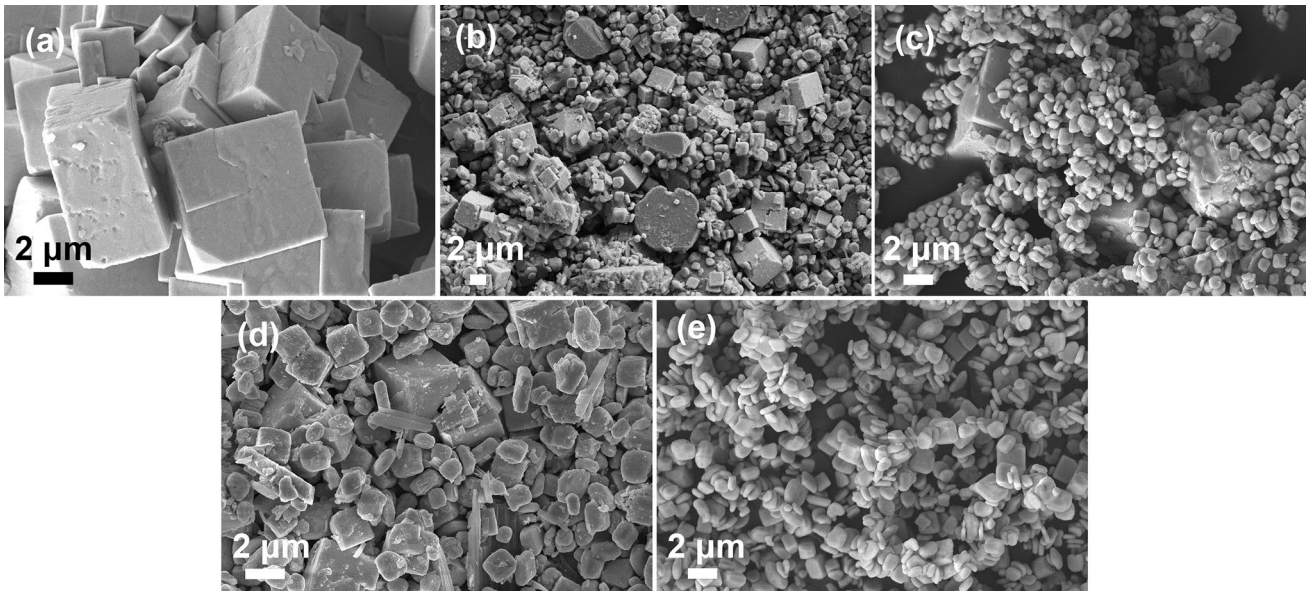

Fig. 3 The FE-SEM micrographs of **a** S1, **b** S2, **c** S3, **d** S4 and **e** S5

Fig. 4 **a** TEM and **b** the corresponding HRTEM image of S3

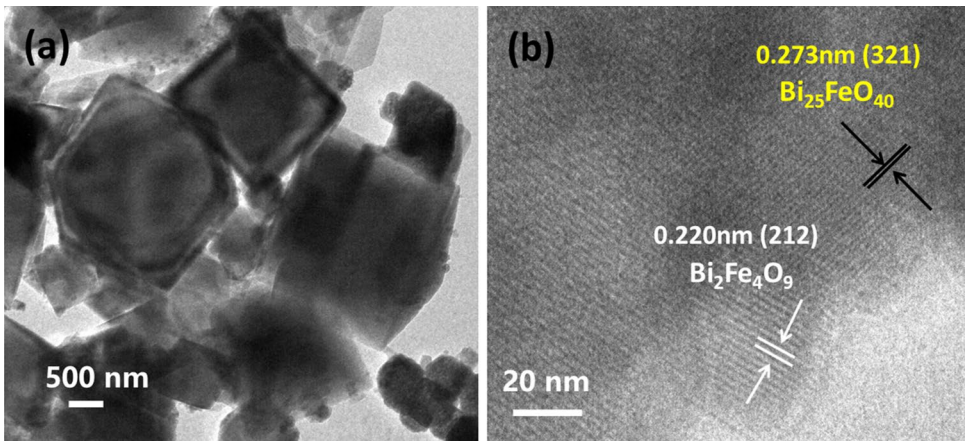

$Bi_{25}FeO_{40}$ and $Bi_2Fe_4O_9$ in the composite [47, 55]. Our SEM and TEM results therefore provide robust evidence that the $Bi_{25}FeO_{40}/Bi_2Fe_4O_9$ composites with the close interfaces are prepared successfully via a hydrothermal process combined with a mixing-calcination method, which could facilitate the separation of photogenerated carriers.

3.3 UV–vis DRS analysis

The optical absorption behaviors of all samples are analyzed via a UV–vis DRS technique, as present in Fig. 5a. It can be seen that both pure $Bi_{25}FeO_{40}$ and $Bi_2Fe_4O_9$ particles respond to visible light in relationship with the absorption edges locating at approximately 640 nm and 670 nm, respectively. Compared with pure $Bi_{25}FeO_{40}$, the composites exhibit not only a redshift in their absorption but also an increase of the absorption intensities as $Bi_2Fe_4O_9$ microsheets gradually cover the surface of $Bi_{25}FeO_{40}$ microcubes, which can be ascribed to the intermolecular interaction between $Bi_2Fe_4O_9$ and $Bi_{25}FeO_{40}$ [15, 56]. It is proven to be beneficial to visible light harvesting and photocatalytic performance improvement [15]. These results imply that all these samples could be regarded as a visible-light-driven semiconductor photocatalysis. Usually, the band gap associated with the UV–vis absorption edge can significantly affect the photocatalytic performance of a semiconductor photocatalysis. According to Kubelka–Munk (K-M) function [44], the band gaps of $Bi_{25}FeO_{40}$ and $Bi_2Fe_4O_9$ can be determined to be 1.94 eV and 1.87 eV using the plot of $(F(R))^{1/2}$ versus the energy ($h\nu$) respectively, as is shown in Fig. 4b. These values are close to those of early reports [16, 30].

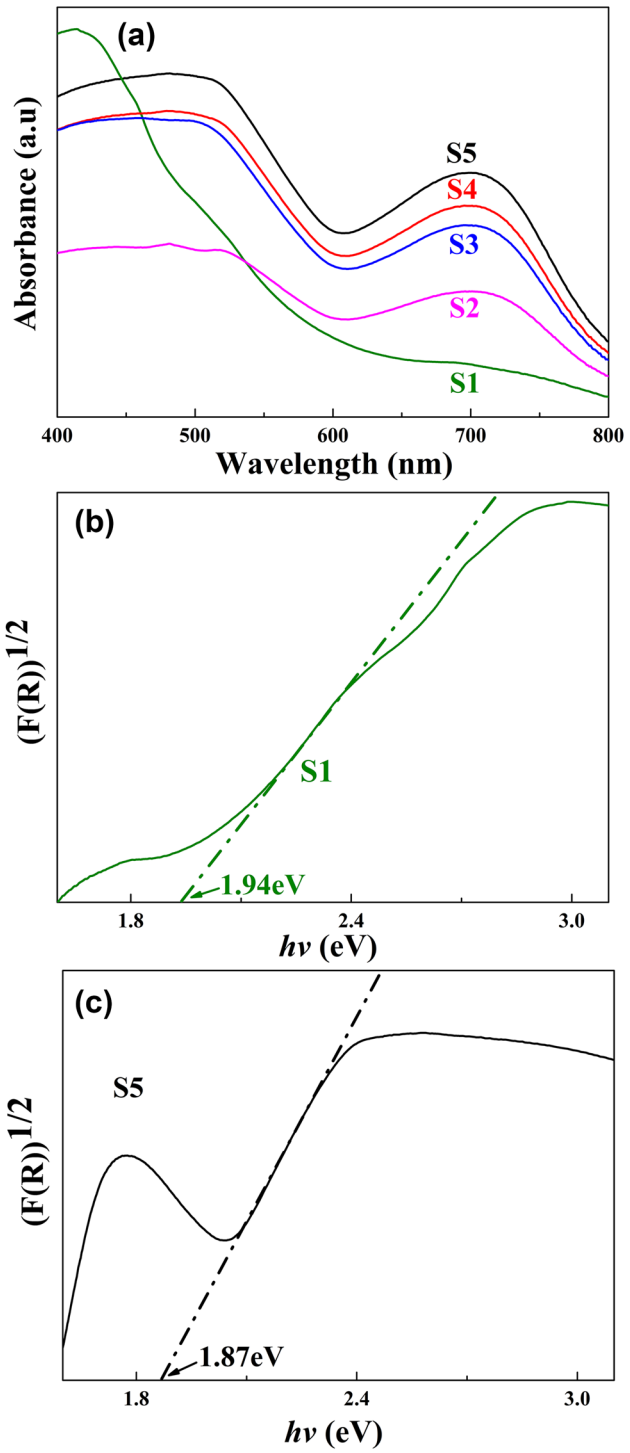

Fig. 5 **a** The UV–vis spectra of as-prepared samples, **b** and **c** are the calculation diagrams of band gaps of S1and S5, respectively

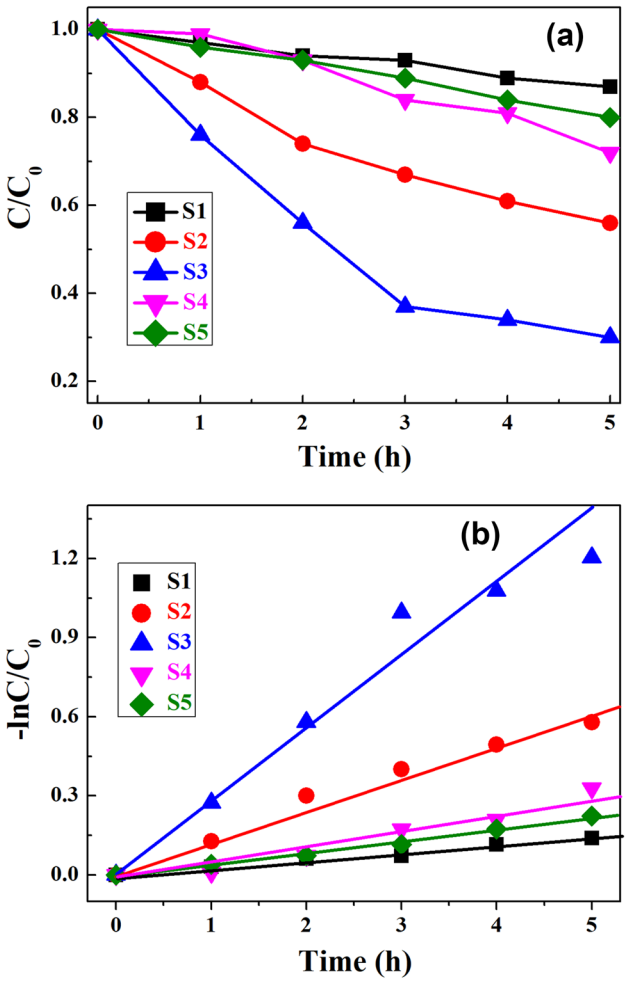

Fig. 6 **a** Visible-light-driven photocatalytic activity of RhB in as-prepared samples within 5 h, **b** the corresponding kinetics of RhB degradation

3.4 Visible-light-driven photocatalytic activities

The visible-light-driven photocatalytic activities of as-prepared samples (S1, S2, S3, S4 and S5) are evaluated by photodegrading RhB under visible-light (Fig. 6a). Pure $Bi_{25}FeO_{40}$ and $Bi_2Fe_4O_9$ powders present poor photocatalytic efficiencies of about 13% and 20% toward RhB within 5 h of reaction, which is mainly due to the strong recombination of photoexcited electron–hole pairs [16, 34, 37]. Compared with either of components, all the $Bi_{25}FeO_{40}$/$Bi_2Fe_4O_9$ composites show significantly enhanced photocatalytic activity of RhB, and their photodegradation efficiencies are 44%, 70% and 28% of S2, S3 and S4 under 5 h visible-light irradiation, respectively. It has been found that 30 wt% of $Bi_2Fe_4O_9$ in the composite (the sample S3) is the optimal loading since it demonstrates the best photocatalytic activity, revealing the synergism between $Bi_{25}FeO_{40}$ and $Bi_2Fe_4O_9$. The synergic effect in the composite will result in the separation of photogenerated carriers and then boost its photocatalytic performance [57]. As shown in the Fig. 6b, the photocatalytic reaction pathways of RhB degradation in all samples approximately follows pseudo-first-order kinetics model [13], and the slope of the

fitting line corresponds to the values of rate constants k. In Fig. 6b, remarkable improvement of photocatalytic activity in $Bi_{25}FeO_{40}/Bi_2Fe_4O_9$ composite is further evidenced. The rate constants k are estimated to be 0.0314 h^{-1}, 0.1221 h^{-1}, 0.2772 h^{-1}, 0.0557 h^{-1} and 0.0449 h^{-1} for the samples S1, S2, S3, S4 and S5, respectively. Moreover, with the increase of $Bi_2Fe_4O_9$ content from 10 to 50%, the photocatalytic efficiencies of composites firstly increase to a maximal value and then decrease. The photocatalytic activity of the sample S3 reaches the maximum at 0.2772 h^{-1}, which is about 8.8 times higher than that of pure $Bi_{25}FeO_{40}$, 6.2 times higher than that of pure $Bi_2Fe_4O_9$, 2.5 times higher than that of the sample S2 and 4.9 times higher than that of the sample S4. The decreased photocatalytic efficiencies of the sample S2 and S4 can be ascribed to the inappropriate amount of $Bi_2Fe_4O_9$ microsheets coving the surface of $Bi_{25}FeO_{40}$ microcubes. Similar phenomena have been also observed in the $Ag_3PO_4/CuBi_2O_4$ and g-$C_3N_4/CeVO_4$ composites [57, 58]. In order to clarify the active radicals working during the photocatalytic process and the related possible photocatalytic mechanism, the active species trapping experiments over $Bi_{25}FeO_{40}/Bi_2Fe_4O_9$ composite have been performed. In this work, different radical scavengers including the 2-propanol (IPA), pbenzoquinone (BQ) and disodium ethylenediamine tetraacetic acid (EDTA-2Na) are used as the quenchers for ·OH, $\cdot O_2^-$ and h^+ respectively. Figure 7 presents the photocatalytic activities of RhB in the sample S3 in the presence of different scavengers. When the IPA is introduced, the photocatalytic efficiencies of RhB decrease from 70 to 36.8%, suggesting that ·OH is the main active species in the composite. However, in the presence of BQ and EDTA-2Na, the photodegradation rate only decreases to 65.6% and 65.1% respectively, indicating that $\cdot O_2^-$ and h^+ have a few impacts on photodegradation of RhB. The above trapping experiments reveal that even though active radicals

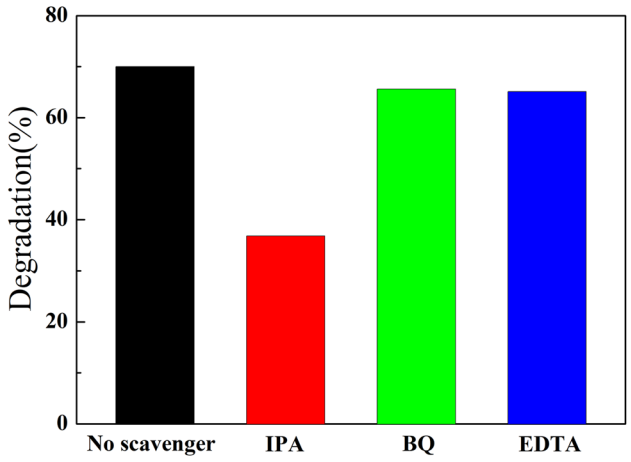

Fig. 7 The active species trapping experiments of the sample S3 during the photocatalytic process

(·OH, $\cdot O_2^-$ and h^+) play roles in the degradation process, the predominant active species for degradation of RhB in $Bi_{25}FeO_{40}/Bi_2Fe_4O_9$ composite is ·OH rather than $\cdot O_2^-$ and h^+. Zhang et al. has also found that ·OH radical is the main active species during the degradation process in $BiFeO_3/Bi_2Fe_4O_9$ heterojunction photocatalysis [7].

3.5 Photocatalytic mechanism

In order to investigate the enhanced photocatalytic performance of $Bi_{25}FeO_{40}/Bi_2Fe_4O_9$ composites, the band-edge potential positions of $Bi_{25}FeO_{40}$ and $Bi_2Fe_4O_9$ photocatalysis are identified by using the famous Mulliken electronegativity theory since band edge play an important role in exploring the generation, separation, and movement pathways of photogenerated charge carriers [46]. The valence band (VB) and conduction band (CB) edge energy can be calculated using the following Eqs. (1) and (2) [50]:

$$E_{VB} = X - E_0 + 0.5\,E_g \quad (1)$$

$$E_{CB} = E_{VB} - E_g \quad (2)$$

In these equations, E_{VB} and E_{CB} are the VB and CB edge potential respectively; X is absolute electronegativity of a semiconductor (the geometric mean of the electronegativity of all constituent atoms, X for $Bi_{25}FeO_{40}$ and $Bi_2Fe_4O_9$ are 6.24 eV and 6.00 eV [34, 59]); E_0 is the energy of free electrons on the hydrogen scale (~4.5 eV); and E_g is the band gap energy for a semiconductor (E_g for $Bi_{25}FeO_{40}$ and $Bi_2Fe_4O_9$ are 1.94 and 1.87 eV vs NHE, respectively). Therefore, the E_{VB} of $Bi_{25}FeO_{40}$ and $Bi_2Fe_4O_9$ are calculated to be 2.71 and 2.44 eV. Accordingly, the E_{CB} of $Bi_{25}FeO_{40}$ and $Bi_2Fe_4O_9$ are 0.77 and 0.57 eV. On the basis of the band alignments of $Bi_{25}FeO_{40}$ and $Bi_2Fe_4O_9$, the schematic diagram of electronic energy-band structure and the heterojunction-type photocatalytic mechanism is proposed in Fig. 8. The scheme shows clearly that the VB top of $Bi_{25}FeO_{40}$ is higher than that of $Bi_2Fe_4O_9$, and the CB bottom of $Bi_{25}FeO_{40}$ is also higher than that of $Bi_2Fe_4O_9$. The electronic band structures of $Bi_{25}FeO_{40}$ and $Bi_2Fe_4O_9$ in the composite match well with each other. Under the visible-light irradiation, both $Bi_2Fe_4O_9$ and $Bi_{25}FeO_{40}$ catalysis can be excited with photogenerated e^-/h^+ carriers due to their suitable bandgap. After coupling $Bi_2Fe_4O_9$ with $Bi_{25}FeO_{40}$, the two semiconductors are closely combined together and consequently the intimate interfaces are formed, as confirmed by our SEM and TEM results. In this manner, the photogenerated holes in the CB of $Bi_{25}FeO_{40}$ will inject into that of $Bi_2Fe_4O_9$ with more positive potential, while the photogenerated electrons in the VB of $Bi_2Fe_4O_9$ will move to that of $Bi_{25}FeO_{40}$ with more negative potential when the composite system is irradiated with visible light, leading to the separation of interfacial electron and holes between $Bi_{25}FeO_{40}$ and $Bi_2Fe_4O_9$. As a

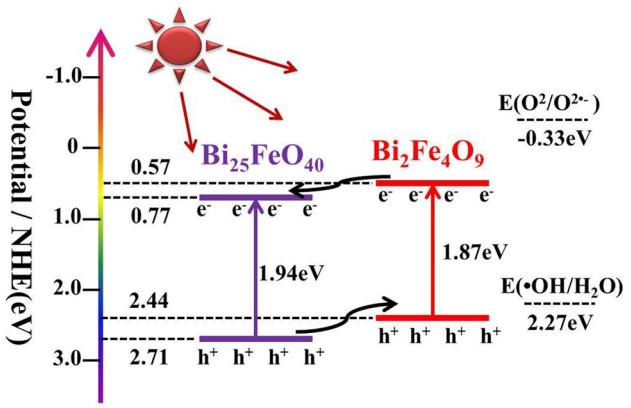

Fig. 8 Schematic illustration of heterojunction-type photocatalytic reaction mechanism in the $Bi_{25}FeO_{40}/Bi_2Fe_4O_9$ interface under visible light irradiation

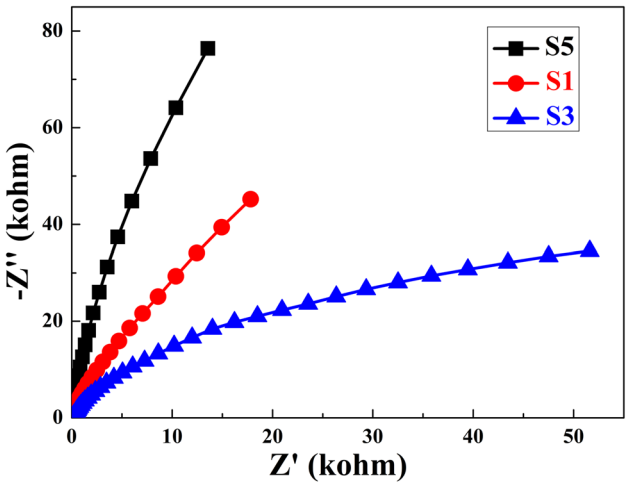

Fig. 9 Comparisons of EIS Nynquist plots of pure $Bi_{25}FeO_{40}$, $Bi_2Fe_4O_9$, and $Bi_{25}FeO_{40}/Bi_2Fe_4O_9$ composites

result, $Bi_{25}FeO_{40}/Bi_2Fe_4O_9$ composite effectively reduces the recombination of photogenerated charge carriers, which is in favor of the enhancement of photocatalytic activity. Recent works also demonstrate that the formation of $BiFeO_3/Fe_2O_3/Bi_2Fe_4O_9$ heterojunction-like interfaces and the mixed-phase $BiFeO_3/Bi_{25}FeO_{40}$ could reduce the electron and holes recombination rate and promote photocatalytic performance [36, 37]. More importantly, the accumulated holes in the CB of $Bi_2Fe_4O_9$ can react with H_2O to produce ·OH groups because the VB potential (2.33 eV) is more positive than that of $\cdot OH/H_2O$ (2.27 eV). The accumulated holes in the CB of $Bi_2Fe_4O_9$ will transfer to the surface of particles and are captured by H_2O molecules adsorbed on the surface of the photocatalysts, producing ·OH radicals to decompose RhB into small molecular products and then into H_2O and CO_2 [60]. However, the accumulated electrons in the CB of $Bi_{25}FeO_{40}$ cannot absorb dissolved O_2 to generate $\cdot O_2^-$ radical that can oxidize RhB due to more positive CB (0.77 eV) than that of $O^2/O^{2\cdot-}$ (−0.33 eV). The photocatalytic process of $Bi_{25}FeO_{40}/Bi_2Fe_4O_9$ composite follows via heterojunction-type mechanism, which is mainly governed by ·OH, rather than by $\cdot O_2^-$ and h^+. The proposed photocatalytic mechanism matches well with our active species trapping experiments. Those above photocatalytic reactions are described as follows:

$$Bi_{25}FeO_{40}/Bi_2Fe_4O_9 + h\nu \rightarrow Bi_2Fe_4O_9\left(e^- + h^+\right) \quad (3)$$

$$h^+ + H_2O \rightarrow \cdot OH + H^+ \quad (4)$$

$$+ Bi_{25}FeO_{40}\left(e^- + h^+\right)$$

$$\cdot OH + RhB \rightarrow H_2O + CO_2 \quad (5)$$

The electrochemical impedance spectra (EIS) measurements is used to affirm the advantage of $Bi_2Fe_4O_9$ over $Bi_{25}FeO_{40}$ composite in the process of photogenerated charge carries separation and migration, as displayed in Fig. 9. The qualitative analysis of EIS can evaluate the electron-transfer efficiency. Generally speaking, the arc radius represents the electron-transfer efficiency; the smaller arc radius in the impedance spectrum is, the higher the separation of photo-excited charge carriers obtained and the quicker the charge transfer across the electrode/electrolyte interface achieved [50]. In Fig. 9, the sample S3 shows a smaller arc radius than that of the pristine $Bi_{25}FeO_{40}$ and $Bi_2Fe_4O_9$, which means a more efficient separation of photogenerated electrons/holes pairs, faster interfacial charge transfer and hence better photocatalytic performance. On the other hand, the transient photocurrent is also believed to be a useful tool to evaluate the separation rate of photogenerated electron–hole pairs in the semiconductor-based photocatalytic composite [46]. The transient photocurrent responses of S1, S3 and S5 samples are recorded over several on–off cycles under visible-light irradiation and shown in Fig. 10. Apparently, the current density of pure $Bi_{25}FeO_{40}$ and $Bi_2Fe_4O_9$ are both 0.04 μA/cm^2 with light on, while the current density of $Bi_{25}FeO_{40}/Bi_2Fe_4O_9$ composite has a great improvement, and it can reach around 0.08 μA/cm^2, which is almost two times than that of pure $Bi_{25}FeO_{40}$ and $Bi_2Fe_4O_9$. These indicate that $Bi_{25}FeO_{40}/Bi_2Fe_4O_9$ composite has the enhanced separation of photogenerated carriers and can thus facilitate its photocatalytic performance.

It is also generally accepted that the optimal weight ratio of every component in composite photocatalyst is related to their geometry architecture, which is essentially beneficial for photocatalytic activity [53]. Based on our SEM and TEM observations, the architecture diagrams of $Bi_{25}FeO_{40}/Bi_2Fe_4O_9$ composites with different weight ratios (the sample S2, S3 and S4) are presented in Fig. 11. When the weight ratio of $Bi_2Fe_4O_9$ to $Bi_{25}FeO_{40}$ is low, the smaller $Bi_2Fe_4O_9$ microsheets are randomly anchored on the surface of the bigger $Bi_{25}FeO_{40}$ microcubes and a large number

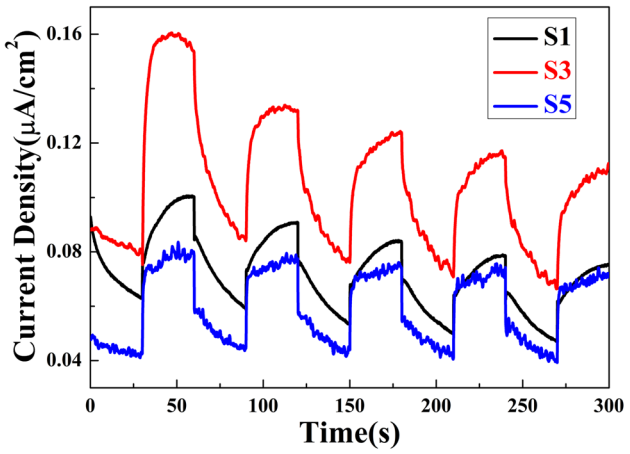

Fig. 10 Transient photocurrent responses of pure $Bi_{25}FeO_{40}$, $Bi_2Fe_4O_9$, and $Bi_{25}FeO_{40}/Bi_2Fe_4O_9$ composites

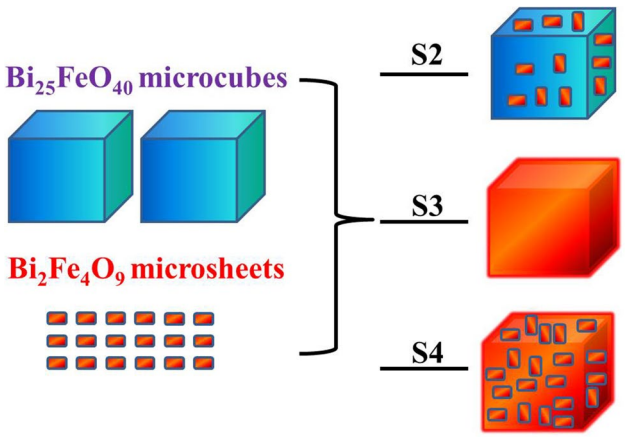

Fig. 11 Architecture sketches of $Bi_{25}FeO_{40}/Bi_2Fe_4O_9$ composites with different weight ratios (S2, S3 and S5 sample)

of surfaces are barren. It means that only a few $Bi_{25}FeO_{40}/Bi_2Fe_4O_9$ heterojunction solid–solid interfaces are formed. Consequently, the efficiency of photogenerated charge carrier separation and transfer cannot be promoted adequately and thus the photocatalytic activity improves a little. When the weight ratio reaches the optimal value, $Bi_2Fe_4O_9$ microsheets uniformly cover the surface of $Bi_{25}FeO_{40}$ microcubes and a thin $Bi_2Fe_4O_9$ layer is formed. The highest visible-light-driven photocatalytic activity in the sample S3 is achieved via this surface structure, which can be explained by the increased number of heterojunctions, enough electron transfer channels and the effective separation of electron–hole pairs [61–66]. However, when the weight ratio further increases, an overlapping surface structure comes into being. The excessive $Bi_2Fe_4O_9$ will reduce the effective heterojunction interfaces, decrease the amount of exposed $Bi_{25}FeO_{40}/Bi_2Fe_4O_9$ heterojunction, depress the active sites on the heterojunction and hinder the utilization efficiency of visible light, all of which damages the photocatalytic activity [7, 44]. In addition, another possible reason is that the thick $Bi_2Fe_4O_9$ layer will extend the electron transfer distance from inner $Bi_{25}FeO_{40}$ to outer $Bi_2Fe_4O_9$, which suppresses the interfacial charge transfer and aggregate the bulk electron–hole recombination [66]. Therefore, the suitable proportion of $Bi_2Fe_4O_9$ to $Bi_{25}FeO_{40}$ will construct the appropriate geometry architecture in the composite, which is one of key issues on the enhancement of photocatalytic properties.

4 Conclusions

In this work, a series of $Bi_{25}FeO_{40}/Bi_2Fe_4O_9$ composite photocatalysis have been constructed via a mixing-calcination method followed by a hydrothermal approach. Among all the samples, the $Bi_{25}FeO_{40}/Bi_2Fe_4O_9$ composite with 30 wt% $Bi_2Fe_4O_9$ loading has the highest visible-light-driven photocatalytic efficiency of about 70% toward RhB within 5 h of reaction. This enhancement could be attributed to heterojunction structure, which can promote the utilization efficiency of visible light, suppress the recombination of interfacial electron-holes pairs, and exacerbate the transfer of photogenerated charge carriers across the interfaces. The mechanism of effects that different weight ratios of $Bi_{25}FeO_{40}/Bi_2Fe_4O_9$ and their geometry architecture have on photocatalytic activity has been revealed. This work provides new insights into the design and development of bismuth ferrite-based visible-light-driven photocatalysis.

Acknowledgements This work was sponsored by the National Natural Science Foundation of China (11704288 and 11504277) and the Scientific Project provided by Wuhan Government (Grant No.: 2016010101010026).

References

1. T. Zhao, A. Scholl, F. Zavaliche, K. Lee, M. Barry, A. Doran et al., Electrical control of antiferromagnetic domains in multiferroic $BiFeO_3$ films at room temperature. Nat. Mater. **5**, 823–829 (2006)
2. D.P. Dutta, A.K. Tyagi, Effect of Sm^{3+} and Zr^{4+} codoping on the magnetic, ferroelectric and magnetodielectric properties of sonochemically synthesized $BiFeO_3$ nanorods. Appl. Surf. Sci. **450**, 429–440 (2018)
3. D. Sando, Y.R. Yang, E. Bousquet, C. Carrétéro, V. Garcia, S. Fusil et al., Large elasto-optic effect and reversible electrochromism in multiferroic $BiFeO_3$. Nat. Commun. **7**, 10718 (2016)
4. A. Kirsch, M.M. Murshed, M. Schowalter, A. Rosenauer, T.M. Gesing, Nanoparticle precursor into polycrystalline $Bi_2Fe_4O_9$: an evolutionary investigation of structural, morphological, optical, and vibrational properties. J. Phys. Chem. C **120**, 18831–18840 (2016)

5. S.D. Waghmare, V.V. Jadhav, S.K. Gore, S.J. Yoon, S.B. Ambade, B.J. Lokhande, R.S. Mane, S.H. Han, Efficient gas sensitivity in mixed bismuth ferrite micro (cubes) and nano (plates) structures. Mater. Res. Bull. **47**, 4169–4173 (2012)
6. S.M. Lam, J.C. Sin, A.R. Mohamed, A newly emerging visible light-responsive $BiFeO_3$ perovskite for photocatalytic applications: a mini review. Mater. Res. Bull. **90**, 15–30 (2017)
7. T. Zhang, Y. Shen, Y.H. Qiu, Y. Liu, R. Xiong, J. Shi et al., Facial synthesis and photoreaction mechanism of $BiFeO_3$/$Bi_2Fe_4O_9$ heterojunction nanofibers. ACS Sustain. Chem. Eng. **5**, 4630–4636 (2017)
8. Q. Zhang, W.J. Gong, J.H. Wang, X.K. Ning, Z.H. Wang, X.G. Zhao, W.J. Ren, Size-dependent magnetic, photoabsorbing, and photocatalytic properties of single-Crystalline $Bi_2Fe_4O_9$ Semiconductor Nanocrystals. J. Phys. Chem. C **115**, 25241–25246 (2011)
9. M.A. Basith, R. Ahsanm, I. Zarin, M.A. Jalil, Enhanced photocatalytic dye degradation and hydrogen production ability of $Bi_{25}FeO_{40}$-rGO nanocomposite and mechanism insight. Sci. Rep. **8**, 11090 (2018)
10. N. Wang, L.H. Zhu, M. Lei, Y.B. She, M.J. Cao, H.Q. Tang, Ligand-induced drastic enhancement of catalytic activity of Nano-$BiFeO_3$ for oxidative degradation of Bisphenol A. ACS. Catal. **1**, 1193–1202 (2011)
11. Z.T. Hu, S.K. Lua, T.T. Lim, Cuboid-like $Bi_2Fe_4O_9$/Ag with Graphene-Wrapping tribrid composite with superior capability for environmental decontamination: nanoscaled material design and visible-light-driven multifunctional catalyst. ACS. Sustain. Chem. Eng. **3**, 2726–2736 (2015)
12. T.L. Wu, L. Liu, M.Y. Pi, D.K. Zhang, S.J. Chen, Enhanced magnetic and photocatalytic properties of $Bi_2Fe_4O_9$ semiconductor with large exposed (001) surface. Appl. Surf. Sci. **377**, 253–261 (2016)
13. H.C. Wang, H.M. Xu, C.C. Zeng, Y. Shen, Y.H. Lin, C.W. Nan, Visible light photocatalytic activity of bismuth ferrites tuned by Bi/Fe Ratio. J. Am. Ceram. Soc. **99**, 1133–1136 (2016)
14. W.D. Ji, M.M. Li, G.K. Zhang, P. Wang, Controlled synthesis of $Bi_{25}FeO_{40}$ with different morphologies: growth mechanism and enhanced photo-Fenton catalytic properties. Dalton Trans. **46**, 10586–10593 (2017)
15. Y. Liu, H.G. Guo, Y.L. Zhang, W.H. Tang, X. Cheng, W. Li, Heterogeneous activation of peroxymonosulfate by Sillenite $Bi_{25}FeO_{40}$: singlet oxygen generation and degradation for aquatic levofloxacin. Chem. Eng. J. **343**, 128–137 (2018)
16. L. Ren, S.Y. Lu, J.Z. Fang, Y. Wu, D.Z. Chen, L.Y. Huang, Enhanced degradation of organic pollutants using $Bi_{25}FeO_{40}$ microcrystals as an efficient reusable heterogeneous photo-Fenton like catalyst. Catal. Today **281**, 656–661 (2017)
17. P. Sharma, D. Varshney, S. Satapathy, P.K. Gupta, Effect of Pr substitution on structural and electrical properties of $BiFeO_3$ ceramics. Mater. Chem. Phys. **143**, 629–636 (2014)
18. J. Silva, A. Reyes, H. Esparza, H. Camacho, L. Fuentes, $BiFeO_3$: a review on synthesis, doping and crystal structure. Inter. Ferroelectr. **126**, 47–59 (2011)
19. S.M. Selbach, M.A. Einarsrud, T. Grande, On the thermodynamic stability of $BiFeO_3$. Chem. Mater. **21**, 169–173 (2009)
20. L. Wu, C.H. Dong, H. Chen, J.L. Yao, C.J. Jiang, D.S. Xue, Hydrothermal synthesis and magnetic properties of bismuth ferrites nanocrystals with various morphology. J. Am. Ceram. Soc. **95**, 3922–3927 (2012)
21. R. Köferstein, Synthesis, phase evolution and properties of phase-pure nanocrystalline $BiFeO_3$ prepared by a starch-based combustion method. J. Alloy. Compd. **590**, 324–330 (2014)
22. H. Béa, M. Bibes, A. Barthélémy, K. Bouzehouane, E. Jacquet, A. Khodan, J.P. Contour et al., Influence of parasitic phases on the properties of $BiFeO_3$ epitaxial thin films. Appl. Phys. Lett. **87**, 72508 (2005)
23. F.E.N. Ramirez, A.C.P. Gabriel, A.S. Jose, Possible misleading interpretations on magnetic and transport properties in $BiFeO_3$ nanoparticles caused by impurity phase. Phys. Lett. A **379**, 1549–1553 (2015)
24. R.Q. Guo, L. Fang, W. Dong, F.G. Zheng, M.R. Shen, Magnetically separable $BiFeO_3$ nanoparticles with a γ-Fe_2O_3 parasitic phase: controlled fabrication and enhanced visible-light photocatalytic activity. J. Mater. Chem. **21**, 18645–18652 (2011)
25. X.F. Wang, W.W. Mao, Q.X. Zhang, Q. Wang, Y.Y. Zhu, J. Zhang et al., PVP assisted hydrothermal fabrication and morphology-controllable fabrication of $BiFeO_3$ uniform nanostructures with enhanced photocatalytic activities. J. Alloy. Compd. **677**, 288–293 (2016)
26. K. Suzuki, Y. Tokudome, H. Tsuda, M. Takahashi, Morphology control of $BiFeO_3$ aggregates via hydrothermal synthesis. J. Appl. Cryst. **49**, 168–174 (2016)
27. T. Gao, Z. Chen, F. Niu, D.T. Zhou, Q.L. Huang et al., Shape-controlled preparation of bismuth ferrite by hydrothermal method and their visible-light degradation properties. J. Alloy. Compd. **648**, 564–570 (2015)
28. C.X. Hao, F.S. Wen, J.Y. Xiang, H. Hou, W.M. Lv, Y.F. Lv et al., Photocatalytic performances of $BiFeO_3$ particles with the average size in nanometer, submicrometer, and micrometer. J. Alloy. Compd. **50**, 369–373 (2014)
29. T. Gao, Z. Chen, Y.X. Zhu, F. Niu, Q.L. Huang, L.S. Qin et al., Synthesis of $BiFeO_3$ nanoparticles for the visible-light induced photocatalytic property. Mater. Res. Bull. **59**, 6–12 (2014)
30. G. Wang, S.H. Yan, J. Sun, S.G. Wang, Q.R. Deng, Visible light photocatalytic and magnetic properties of Nd doped $Bi_2Fe_4O_9$ powders. J. Mater. Sci.: Mater. Electron. **28**, 4371–4377 (2017)
31. Y.L. Pei, C.L. Zhang, Effect of ion doping in different sites on the morphology and photocatalytic activity of $BiFeO_3$ microcrystals. J. Alloy. Compd. **570**, 57–60 (2013)
32. M. Sakar, S. Balakumar, P. Saravanan, S. Bharathkumar, Particulates vs fibers: dimension featured magnetic and visible light driven photocatalytic properties of Sc modified multiferroic bismuth ferrite nanostructures. Nanoscale **8**, 1147–1160 (2016)
33. X. Yang, Y.F. Zhang, G. Xu, X. Wei, Z.H. Ren, G. Shen et al., Phase and morphology evolution of bismuth ferrites via hydrothermal reaction route. Mater. Res. Bull. **48**, 1694–1699 (2013)
34. G.M. Wang, C. Lin, S.T. Liu, Q.R. Deng, Y.W. Mao, S.G. Wang, Hydrothermal synthesis of bismuth ferrite with controllable phase structure, morphology and visible light photocatalytic activities. J. Mater. Sci. **29**, 4926–4932 (2018)
35. J.J. Kong, Z.B. Rui, X.Y. Wang, H.B. Ji, Y.X. Tong, Visible-light decomposition of gaseous toluene over $BiFeO_3$-$(Bi/Fe)_2O_3$ heterojunctions with enhanced performance. Chem. Eng. J. **302**, 552–559 (2016)
36. T.A. Gadhi, S. Hernández, M. Castellino, A. Chiodoni, T. Husak, G. Barrera et al., Single $BiFeO_3$ and mixed $BiFeO_3$/Fe_2O_3/$Bi_2Fe_4O_9$ ferromagnetic photocatalysts for solar light driven water oxidation and dye pollutants degradation. J. Ind. Eng. Chem. **63**, 437–448 (2018)
37. S. Kalikeri, V.S. Kodialbail, Solar light-driven photocatalysis using mixed-phase bismuth ferrite ($BiFeO_3$/$Bi_{25}FeO_{40}$) nanoparticles for remediation of dye-contaminated water: kinetics and comparison with artificial UV and visible light-mediated photocatalysis. Environ. Sci. Pollut. R **25**, 13881–13893 (2018)
38. C. Wang, H.Q. Fan, X.H. Ren, Y. Wen, W.J. Wang, Highly dispersed PtO nanodots as efficient co-catalyst for photocatalytic hydrogen evolution. Appl. Surf. Sci. **462**, 423–431 (2018)
39. M.C. Zhang, H.Q. Fan, N. Zhao, H.J. Peng, X.H. Ren, W.J. Wang et al., 3D hierarchical $CoWO_4$/Co_3O_4nanowire arrays for

asymmetric supercapacitors with high energy density. Chem. Eng. J. **347**, 291–300 (2018)
40. H.L. Tian, H.Q. Fan, J.W. Ma, L.T. Ma, G.Z. Dong, Noble metal-free modified electrode of exfoliated graphitic carbon nitride/ZnO nanosheets for highly efficient hydrogen peroxide sensing. Electrochim. Acta **247**, 787–794 (2017)
41. Y.W. Zhao, H.Q. Fan, K. Fu, L.T. Ma, M.M. Li, J.W. Fang, Intrinsic electric field assisted polymeric graphitic carbon nitride coupled with $Bi_4Ti_3O_{12}/Bi_2Ti_2O_7$ heterostructure nanofibers toward enhanced photocatalytic hydrogen evolution. Int. J. Hydrog. Energy **41**, 16913–16926 (2016)
42. Y.M. Xia, Z.M. He, J.B. Su, Y. Liu, B. Tang, X.P. Li, Fabrication of novel n-$SrTiO_3$/p-BiOI heterojunction for degradation of crystal violet under simulated solar light irradiation. NANO **13**, 1850070 (2018)
43. M.J. Liang, Z.Y. Yang, Y. Yang, Y. Mei, H.R. Zhou, S.J. Yang, One-step introduction of metallic Bi and non-metallic C in Bi_2WO_6 with enhanced photocatalytic activity. J. Mater. Sci. **30**, 1310–1321 (2019)
44. G.M. Wang, S.T. Liu, T.C. He, X. Liu, Q.R. Deng, Y.W. Mao, Enhanced visible-light-driven photocatalytic activities of $Bi_2Fe_4O_9$/g-C_3N_4 composite photocatalysts. Mater. Res. Bull. **104**, 104–111 (2018)
45. H. Wang, S. Liu, Y.L. Zhao, J.N. Niu, P.Z. Feng, Enhanced photocatalytic activity and photostability for novel g-C_3N_4 decorated Bi_2O_4 microrod composites. Mater. Res. Bull. **89**, 253–262 (2017)
46. B.S. Li, C. Lai, G.M. Zeng, L. Qin, H. Yi, D.L. Huang et al., Facile hydrothermal synthesis of Z-scheme Bi2Fe4O9/Bi2WO6 heterojunction photocatalyst with enhanced visible light photocatalytic activity. ACS. Appl. Mater. Inter. **10**, 18824–18836 (2018)
47. L. Zhang, Y. Zou, J. Song, C.L. Pan, S.D. Sheng, C.M. Hou et al., Enhanced photocatalytic activity of $Bi_{25}FeO_{40}$-Bi_2WO_6 heterostructures based on the rational design of the heterojunction interface. RSC. Adv. **6**, 26038–26044 (2016)
48. Z.T. Hu, Z. Chen, R. Goei, W.Y. Wu, T.T. Lim, Magnetically recyclable Bi/Fe-based hierarchical nanostructures via self-assembly for environmental decontamination. Nanoscale **8**, 12736–12746 (2016)
49. H. Zhang, T. Tong, J.G. Chen, J.R. Cheng, Synthesis and visible light photocatalytic properties of $Bi_2Fe_4O_9$ particles via EDTA-assisted sol–gel route. J. Sol-Gel. Sci. Technol. **78**, 135–143 (2016)
50. H.P. Li, J.Y. Liu, W.G. Hou, N. Du, R.J. Zhang, X.T. Tan, Synthesis and characterization of g-C_3N_4/Bi_2MoO_6 heterojunctions with enhanced visible light photocatalytic activity. Appl. Catal. B-Environ. **160**, 89–97 (2014)
51. T.T. Li, L.H. Zhao, Y.M. He, J. Cai, M.F. Luo, J.J. Lin, Synthesis of g-C_3N_4/$SmVO_4$ composite photocatalyst with improved visible light photocatalytic activities in RhB degradation. Appl. Catal. B **129**, 255–263 (2013)
52. T. Fan, C.C. Chen, Z.H. Tang, Y. Ni, C.H. Lu, Synthesis and characterization of g-C_3N_4/$BiFeO_3$ composites with an enhanced visible light photocatalytic activity. Mater. Sci. Semicond. Process. **40**, 439–445 (2015)
53. P. Zhou, J.G. Yu, M. Jaroniec, All-solid-state Z-scheme photocatalytic systems. Adv. Mater. **26**, 4920–4935 (2014)
54. R.M. Cong, H.Q. Yu, Y.J. Luo, J. Li, W.W. Wang, Q.H. Li et al., Synthesis and properties of $Bi_{25}FeO_{40}/\alpha$-Fe_2O_3 composite nanoparticle photocatalysts. Chem. J. Chin. U. **39**, 629–635 (2018)
55. Q.L. Xu, B.C. Zhu, C.J. Jiang, B. Cheng, J.G. Yu, Constructing 2D/2D Fe_2O_3/g-C_3N_4 direct Z-Scheme photocatalysts with enhanced H_2 generation performance. Sol. RRL. **2**, 1800006 (2018)
56. L. Ge, C.C. Han, J. Liu, Novel visible light-induced g-C_3N_4/Bi_2WO_6 composite photocatalysts for efficient degradation of methyl orange. Appl. Catal. B **108–109**, 100–107 (2011)
57. W.L. Shi, F. Guo, S.L. Yuan, In situ synthesis of Z-scheme $Ag_3PO_4/CuBi_2O_4$ photocatalysts and enhanced photocatalytic performance for the degradation of tetracycline under visible light irradiation. Appl. Catal. B **209**, 720–728 (2017)
58. L. Li, H.R. Wang, X. Wang, $CeVO_4$ nanofibers hybridized with g-C_3N_4 nanosheets with enhanced visible-light-driven photocatalytic activity. Solid State Commun. **269**, 11–15 (2018)
59. M.M. Lv, H.B. Yang, Y.L. Xu, Q. Chen, X.T. Liu, F.Y. Wei, Improving the visible light photocatalytic activities of $Bi_{25}FeO_{40}$/MIL-101/PTH via polythiophene wrapping, J. Envirom. Chem. Eng. **3**, 1003–1008 (2015)
60. L.J. Song, Y.J. Zheng, C.F. Chen, Sonication-assisted deposition–precipitation synthesis of graphitic C_3N_4/BiOCl heterostructured photocatalysts with enhanced rhodamine B photodegradation activity. J. Mater. Sci. **28**, 15861–15869 (2017)
61. F. Niu, D. Chen, L.S. Qin, N. Zhang, J.Y. Wang, Z. Chen et al., Facile synthesis of highly efficient p–n heterojunction CuO/$BiFeO_3$ composite photocatalysts with enhanced visible-light photocatalytic activity. ChemCatChem. **7**, 3279–3289 (2015)
62. L. Ge, C.C. Han, J. Liu, Novel visible light-induced g-C_3N_4/Bi_2WO_6 composite photocatalysts for efficient degradation of methyl orange. Appl. Catal. B **108**, 100–107 (2011)
63. D.H. Xia, W.J. Wang, R. Yin, Z.F. Jiang, T.C. An, G.Y. Li et al., Enhanced photocatalytic inactivation of Escherichia coli by a novel Z-scheme g-C_3N4/m-Bi_2O_4 hybrid photocatalyst under visible light: the role of reactive oxygen species. Appl. Catal. B **214**, 23–33 (2017)
64. Z.T. Liu, L.H. Zhang, M. Shao, Y. Wu, D. Zeng, X. Cai et al., Fine-tuning the quasi-3D geometry: enabling efficient nonfullerene organic solar cells based on perylene diimides. ACS Appl. Mater. Interfaces. **10**, 762–768 (2018)
65. Z.T. Liu, X.L. Zhang, P.C. Li, X. Gao, Recent development of efficient A-D-A type fused-ring electron acceptors for organic solar. Sol. Energy **174**, 171–188 (2018)
66. J.G. Yu, S.H. Wang, J.X. Low, W. Xiao, Enhanced photocatalytic performance of direct Z-scheme g-C_3N_4-TiO_2 photocatalysts for the decomposition of formaldehyde in air. Phys. Chem. Chem. Phys. **15**, 16883–16890 (2013)

Publisher's Note Springer Nature remains neutral with regard to jurisdictional claims in published maps and institutional affiliations.